Outer hair cell electromechanical properties in a nonlinear piezoelectric model

Yi-Wen Liu[a] and Stephen T. Neely
Boys Town National Research Hospital, 555 North 30th Street, Omaha, Nebraska 68131

(Received 30 December 2008; revised 27 March 2009; accepted 27 May 2009)

A nonlinear piezoelectric circuit is proposed to model electromechanical properties of the outer hair cell (OHC) in mammalian cochleae. The circuit model predicts (a) that the nonlinear capacitance decreases as the stiffness of the load increases, and (b) that the axial compliance of the cell reaches a maximum at the same membrane potential for peak capacitance. The model was also designed to be integrated into macro-mechanical models to simulate cochlear wave propagation. Analytic expressions of the cochlear-partition shunt admittance and the wave propagation function are derived in terms of OHC electro-mechanical parameters. Small-signal analyses indicate that, to achieve cochlear amplification, (1) nonlinear capacitance must be sufficiently high and (2) the OHC receptor current must be sensitive to the velocity of the reticular lamina.
 [DOI: 10.1121/1.3158919]

PACS number(s): 43.64.Kc, 43.64.Ld [BLM] Pages: 751–761

I. INTRODUCTION

The outer hair cells (OHCs) in mammalian cochleae are thought to provide a feedback that results in cycle-by-cycle amplification of traveling waves (Patuzzi, 1996; Robles and Ruggero, 2001; Dallos, 2008). This amplification has been considered necessary to account for the fine tuning and high sensitivity of hearing (Shera, 2007). Two "active" mechanisms possibly contribute to this amplification: (1) a hair-bundle (HB) motility generated during mechano-electrical transduction (MET) (Hudspeth, 1997) and (2) a somatic motility generated by protein motors embedded in the lateral membrane (Brownell *et al.*, 1985; Ashmore, 1987). Both mechanisms are nonlinear: the force generated by the electromotile HB is a nonlinear function of HB deflection angle (Fettiplace *et al.*, 2006) and the contraction and the gating charge due to the electromotile membrane are both a nonlinear function of trans-membrane voltage (Santos-Sacchi, 1991).

Nonlinear micro-mechanical models have been constructed to describe HB motility (e.g., Tinevez *et al.*, 2006) and somatic motility (Iwasa and Adachi, 1997; Spector *et al.*, 1999), respectively. Recently, nonlinearity in HB motility has been incorporated in simulations of cochlear mechanics (Ramamoorthy *et al.*, 2007; Lu *et al.*, 2009). Nonlinearity in somatic motility, however, was ignored in these studies. This paper presents a step toward assessing the role of nonlinear OHC somatic motility in cochlear mechanics. A nonlinear piezoelectric membrane model is presented. The model captures various features in OHC somatic motility and can be integrated with cochlear models to simulate interaction between OHC and surrounding structures at auditory frequencies.

Mountain and Hubbard (1994) first proposed to model OHC somatic motility as a piezoelectric effect. Electromotility was represented by an ideal piezoelectric transformer. The transformer converts voltage to force and couples gating charge to axial contraction. The original model, being linear and one-dimensional, has been extended to describe the nonlinearity in electromotility (Iwasa and Adachi, 1997; Spector *et al.*, 1999) and the anisotropic stress-strain relations of the lateral wall (Tolomeo and Steele, 1995; Iwasa and Adachi, 1997). More recent theoretic extensions include a high-frequency resonance due to coupling between electrical and mechanical waves within the lateral wall (Weitzel *et al.*, 2003) and OHC volume non-conservation in slower processes (Allen and Fahey, 2006). Foundation of OHC piezoelectricity in statistical mechanics was also described (Iwasa, 2001). A comprehensive review of OHC membrane electromechanical models was given by Spector *et al.* (2006).

Piezoelectric membrane models have been incorporated into cochlea models (Lu *et al.*, 2006; Ramamoorthy *et al.*, 2007; Lu *et al.*, 2009) to simulate auditory tuning curves (Ruggero *et al.*, 1990; de Boer and Nuttall, 2000; Cooper, 1998; Ren and Nuttall, 2001). Using control theory, Lu *et al.* (2006) explained how an electrically low-pass OHC membrane would allow traveling waves to amplify at higher frequencies. For simplicity, all the electro-mechanical parameters were kept linear. Ramamoorthy *et al.* (2007) and Lu *et al.* (2009) introduced nonlinearity to the MET in their models. Both studies correctly simulated the broadening of cochlear tuning and the decrease in gain as intensity of the stimuli increases. However, the role of nonlinear somatic motility in cochlear tuning remains unexplored.

The two sources of motility have different positions in the OHC feedback loop. Relative to the OHC filter (Neely, 1985), HB motility must be placed before it, and somatic motility, after. Numerical simulation has shown that the spectral distribution of harmonic distortion is sensitive to the position of nonlinearity in the feedback loop (How *et al.*, 2009). Thus, it is conceivable that nonlinearities in HB motility and somatic motility may also have different contribution to other phenomena in cochlear signal processing.

[a]Author to whom correspondence should be addressed. Electronic mail: liuy@boystown.org

Therefore, it is desirable to model nonlinearities separately in the two sources of OHC motility so as to study macroscopic phenomena in cochlear mechanics.

This paper reports a step toward this goal. An OHC membrane model is proposed in Sec. II and an equivalent circuit diagram is shown. Nonlinear analyses of the circuit are performed, and results are compared to experimental data for nonlinear capacitance and voltage-dependent cell compliance. Section III demonstrates how the model can be integrated with a model of the cochlear partition, and tuning properties near the hearing threshold are derived via a small-signal analysis. In Sec. IV, OHC physiological conditions for traveling-wave amplification are further explored. The present model is compared to previous models, and discussions are given in Sec. V.

II. THE PROPOSED MEMBRANE MODEL AND ITS PREDICTIONS

In this section, an equivalent circuit model for the OHC membrane is presented. The circuit represents a relation between the OHC receptor current i_r and the membrane potential V. It predicts a stiffness-dependent nonlinear capacitance and a voltage-dependent compliance, and results are compared to experimental data.

A. Construction of a circuit diagram

First, let us assume that the OHC membrane has a dielectric capacitance C and a leakage conductance G. Thus, i_r can be written as the following:

$$i_r = GV + C\frac{dV}{dt} + i_d, \tag{1}$$

where i_d denotes a gating current due to charge displacement induced by conformational change in the membrane motors. Let $Q=\int i_d dt$ denote this charge and assume that Q is linearly coupled to OHC motility ξ_o:

$$\xi_o = TQ. \tag{2}$$

Here, a positive ξ_o represents a reduction in the length of OHC, and the coefficient T can be regarded as a piezoelectric transformer ratio (Mountain and Hubbard, 1994). Throughout this paper, T is defined as a constant independent of V. Further, assume that Q is a nonlinear function of V and an internal tensile force f_{OHC}:

$$Q = \frac{Q_{\max}}{1+\exp[-(V - Tf_{\mathrm{OHC}} - v_0)/v_1]}. \tag{3}$$

Here, $Q_{\max}$ is the maximum gating charge, and v_0 and v_1 determine the midpoint and the slope of $Q(V)$, respectively. Equation (3) is a consequence of a one-dimensional thermodynamic model and its derivation is given in the Appendix.

All the equations above can be summarized by the circuit diagram shown in Fig. 1, where $\dot{\xi}_o$ denotes the OHC contraction velocity, K denotes a static OHC axial stiffness, and Z represents a mechanical impedance if there is any external load.

This circuit is similar to that of Mountain and Hubbard (1994),[1] except that the gating current i_d charges a nonlinear capacitor in series with an ideal transformer. The circuit diagram is drawn this way to be consistent with the assumption that Q is a nonlinear function of $V-Tf_{\mathrm{OHC}}$ in Eq. (3).

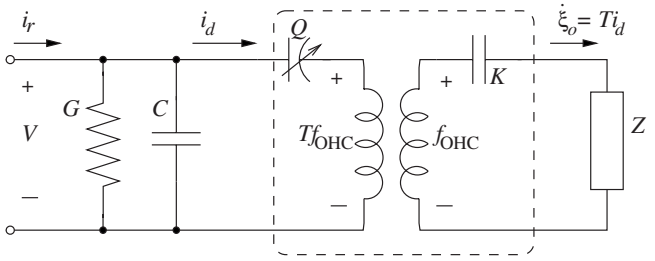

FIG. 1. The proposed circuit model of the OHC lateral membrane. The dashed box represents a nonlinear piezoelectric component. It is connected to the electrical domain on the left and the mechanical domain on the right (symbols are defined in the text).

It should be clarified that the piezoelectric component is always subject to the full membrane potential V. Nevertheless, it is useful to think of V as the sum of $V-Tf_{\mathrm{OHC}}$ and Tf_{OHC}. The advantage of such thinking will become more obvious when conducting small-signal analyses in Secs. III and IV.

At this point, an observation can be made: if the mechanical impedance of OHC is so small that $Tf_{\mathrm{OHC}} \ll V$, the membrane capacitance will be measured as the sum of a constant C and a nonlinear part $C_{\mathrm{NL}}=\partial Q/\partial V$. Since $Q(V)$ is a Boltzmann function in Eq. (3), its derivative $C_{\mathrm{NL}}(V)$ is bell-shaped. This agrees qualitatively with patch-clamp measurements in isolated OHCs (e.g., Santos-Sacchi, 1991). However, if the mechanical impedance Z is not negligible, the *nonlinear capacitance* C_{NL} can be computed as described next.

B. Nonlinear capacitance

First, let us assume that C_{NL} is measured by sweeping the voltage V slowly so that the mechanical impedance Z is stiffness-dominated. Denote the stiffness of Z as K_p. Thus, Hooke's law defines a relation between force f_{OHC} and displacement ξ_o as the following:

$$f_{\mathrm{OHC}} = (K + K_p)\xi_o. \tag{4}$$

Combining Eqs. (2)–(4), the following relation between Q and V is obtained:

$$Q = \frac{Q_{\max}}{1+\exp[-(V - T^2(K+K_p)Q - v_0)/v_1]}. \tag{5}$$

Note that the variable Q occurs on both sides of Eq. (5); the equation is transcendental and $Q(V)$ can only be solved numerically. Finally, C_{NL}, by definition, can be computed by taking the first derivative of Q with respect to V:

$$C_{\mathrm{NL}} \triangleq \frac{\partial Q}{\partial V}. \tag{6}$$

The function $Q(V)$ is plotted in Fig. 2(a) for three different values of stiffness: $K_p=0$ represents an OHC in isolation, $K_p=0.05$ N/m is typical of a fiber-glass probe contacting the OHC during a certain kind of measurement (e.g., Hallworth, 2007), and $K_p=0.15$ N/m is typical of OHC *in*

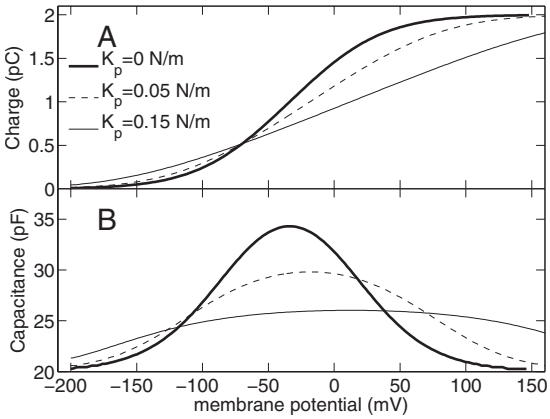

FIG. 2. (A) Gating charge and (B) the sum of C and C_{NL} as a function of membrane potential. Both functions are plotted using three different values of load stiffness K_p=0, 0.05, or 0.15 N/m. Other OHC parameters are K =0.02 N/m, $Q_{\max}$=2 pC, $T=8\times10^5$ m/C, v_0=−40 mV, and v_1=28.6 mV.

situ [see stiffness of reticular-lamina (RL), denoted as K_r in Table I]. Results show that, at a higher K_p, $Q(V)$ is more spread-out.

The sum of C and C_{NL} is shown in Fig. 2(b) as a function of V. Similar to $Q(V)$, it is more spread-out for a higher value of K_p. The peak capacitance decreases and the peak voltage shifts to the right as K_p increases.

In the extreme case when K_p approaches infinity,$C_{\mathrm{NL}}(V)$ should approach zero because the external load is too stiff for the OHC to make any contraction. This has been experimentally observed by Adachi and Iwasa (1999). However, the decrease in peak capacitance was not accompanied by a shift in peak voltage. This discrepancy can be resolved by considering mechanical orthotropy in a two-dimensional membrane model (Iwasa and Adachi, 1997). Here, the shift in peak voltage should be seen as an artifact due to one-dimensional approximation of membrane elasticity in the present model.

C. Voltage-dependence of cell compliance

There has been a dispute over the voltage-dependence of the axial stiffness of OHC. The axial stiffness decreased as a function of membrane potential in an experiment conducted by He and Dallos (1999). A thermodynamic model was constructed to explain this result (Deo and Grosh, 2004). However, no correlation was found between the cell compliance (inverse of stiffness) and membrane potential in a more recent experiment (Hallworth, 2007).

It would be an interesting exercise to see whether the present model predicts a voltage-dependence of the OHC axial compliance. First, by multiplying Eq. (3) by T, OHC contraction can be written as the following:

$$\xi_o = \frac{TQ_{\max}}{1+\exp[-(V-Tf_{\mathrm{OHC}}-v_0)/v_1]}. \tag{7}$$

Further, let us assume that a small external force f_{ext} is applied in order to measure the cell compliance. The external force reduces the internal tensile force f_{OHC} from its static value $f^{(0)}$; that is,

$$f_{\mathrm{OHC}} = f^{(0)} - f_{\mathrm{ext}}. \tag{8}$$

Consequently, the total contraction ξ_{tot} due to f_{ext} is given by the following:

TABLE I. List of parameters and their values used in simulation.

Symbol	Meaning (unit)	Value
	Organ of Corti mechanical parameters	
M_r	Mass of RL system (kg)	2.0×10^{-10}
K_r	Stiffness of RL system (N/m)	0.175
R_r	Damping of RL system (kg/s)	$(\sqrt{M_rK_r}/4.0)$[a]
M_b	Mass of BM system (kg)	2.0×10^{-10}
K_b	Stiffness of BM system (N/m)	1.2
R_b	Damping of BM system (kg/s)	$(\sqrt{M_bK_b}/6.0)$[a]
	Outer hair cell electro-mechanical properties	
T	Piezoelectric transformer ratio (m/C)	(8×10^5)[b]
G	Membrane conductance (nS)	50
C	Membrane capacitance (pF)	20
$\tilde{c}$	Small-signal equivalent capacitance (pF)	15
α_d	Receptor current's sensitivity to RL displacement (A/m)	(0.02)[c]
α_{v0}	Receptor current's sensitivity to RL velocity (C/m)	(2.5×10^{-6})[c]
K	Static axial stiffness (N/m)	(0.02)[d]
	Physical dimensions	
A	Cochlear cross-sectional area (cm^2)	0.01
W	BM width (cm)	0.1
D	Spacing of OHC in the wave-traveling direction (μm)	15

[a]Lu *et al.* (2006).
[b]Mountain and Hubbard (1994).
[c]See Sec. V C for comparison to an estimate from Fettiplace *et al.* (2006).
[d]Hallworth (2007).

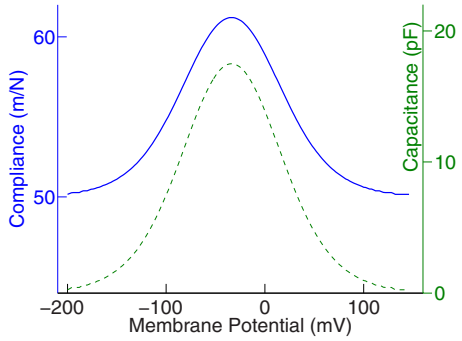

FIG. 3. (Color online) Cell compliance B (solid line) and small-signal equivalent capacitance $\tilde{c}$ (dashed line) as a function of membrane potential. Parameter values are $K=0.02$ N/m, $Q_{\max}=2$ pC, $v_0=-40$ mV, and $v_1=28.6$ mV.

$$\xi_{\text{tot}} = \frac{f_{\text{ext}}}{K} + \frac{TQ_{\max}}{1+\exp[-(V-Tf_{\text{OHC}}-v_0)/v_1]} = \frac{f_{\text{ext}}}{K} + \frac{TQ_{\max}}{1+\exp[-(V-Tf^{(0)}+Tf_{\text{ext}}-v_0)/v_1]},$$

and the cell compliance B can be calculated in the following way:

$$B \triangleq \frac{\partial \xi_{\text{tot}}}{\partial f_{\text{ext}}} = \frac{1}{K} + T\frac{\partial Q}{\partial \tilde{v}}\frac{\partial \tilde{v}}{\partial f_{\text{ext}}} = \frac{1}{K} + T^2\frac{\partial Q}{\partial \tilde{v}}.$$

In the preceding equation, $\tilde{v}$ denotes $V-Tf_{\text{OHC}}$ and can be regarded as an equivalent voltage across the nonlinear capacitor in Fig. 1. Therefore, $\partial Q/\partial \tilde{v}$ can be regarded as a small-signal equivalent capacitance of that capacitor $\tilde{c}$,

$$\tilde{c} \triangleq \frac{\partial Q}{\partial \tilde{v}} = \frac{Q_{\max}}{v_1}\cdot\frac{\theta}{(1+\theta)^2}, \tag{9}$$

where $\theta=\exp[-(V-Tf_{\text{OHC}}-v_0)/v_1]$. Consequently, B can be written as

$$B = \frac{1}{K} + T^2\tilde{c}. \tag{10}$$

It must be clarified that $\tilde{v}$ is a mathematical construct and it cannot be measured experimentally. The membrane motors are always subject to the full potential V and it is C_{NL} that is measured experimentally, not $\tilde{c}$.

Nevertheless, $\tilde{c}$ is a convenient term that will occur repeatedly in Secs. III and IV when analyzing OHC feedback and tuning. In Fig. 3, B and $\tilde{c}$ are shown as a function of V. According to Eq. (10), the cell compliance amount that can change with membrane potential is $T^2\tilde{c}(V)$. As shown in Fig. 3, the maximum compliance increment of 11 m/N corresponds to $\tilde{c}$ of 17 pF if $T=8\times10^5$ m/C.

This increment of 11 m/N in cell compliance corresponds to a fractional change of 0.22 for a hypothetical OHC with a static compliance K^{-1} of 50 m/N. The fractional compliance change reported by He and Dallos (1999) was about six to seven times greater than 0.22. Also, it increased monotonically as a function of membrane potential, whereas the present model predicts that the compliance reaches a maximum at approximately −40 mV. The present prediction is similar to a previous prediction by Iwasa [2001, Fig. 3(A)]. Implications of the discrepancy between the present model's prediction and He and Dallos's (1999) data are further discussed in Sec. V B.

Hallworth's (2007) data [2007, Fig. 3(c)], however, showed a smaller fractional compliance change in the range of −0.4 to +0.5. Most of the data points were scattered between ±0.25. Hallworth's (2007) fractional compliance change is comparable to what the present model predicts, but it did not have a single maximum as a function of voltage. Neither did it increase monotonically as a function of membrane potential. The fractional compliance change predicted by the present model, at most 0.22 if it exists, might be too small to have been observed by Hallworth (2007).

III. SMALL-SIGNAL ANALYSIS OF OHC FEEDBACK

Despite the partial success in explaining electromechanical properties experimentally, this section proceeds to integrate the present model with macro-mechanical cochlear models and calculate OHC feedback. Here and in Sec. IV, analyses will be conducted under the *small-signal* assumption; in other words, stimuli and responses are assumed to have small magnitudes so that the system is represented well by its linear approximation.

For the convenience of discussion, the OHC feedback is characterized by a transfer function $H_o(s)$ that relates OHC contraction to RL displacement,

$$H_o(s) = \xi_o(s)/\xi_r(s), \tag{11}$$

where $s=j\omega$ denotes the frequency variable in Laplace transform. $H_o(s)$ can be regarded as an open-loop displacement gain produced by the OHC. To calculate it, first, note that Eq. (2) relates ξ_o to i_d in the following way:

$$\xi_o = Ti_d/s, \tag{12}$$

where the factor $1/s$ represents integration with respect to time. Subsequently, i_d is related to i_r based on Kirchhoff's principle:

$$i_d = i_r\frac{(1/s\tilde{c}+Z_{\text{eq}})^{-1}}{(G+sC)+(1/s\tilde{c}+Z_{\text{eq}})^{-1}}. \tag{13}$$

In the preceding equation, $Z_{\text{eq}}=T^2(Z+s^{-1}K)$ denotes an equivalent electrical impedance due to mechanical load impedance Z and OHC static stiffness K. Finally, the receptor current i_r can be related to ξ_r by assuming that

$$i_r = (s\alpha_v+\alpha_d)\xi_r. \tag{14}$$

In the preceding equation, α_v and α_d represent a velocity-to-current and a displacement-to-current gain, respectively. Note that i_r responds to HB deflection in reality (e.g., Fettiplace *et al.*, 2006), but interaction between HB and the tectorial membrane (TM) is not modeled here in Eq. (14). Two different ways to interpret the equation will be given in Sec. V C.

Combining Eqs. (12)–(14), the transfer function $H_o(s)$ can be written as

$$H_o(s) = \frac{T(s\alpha_v+\alpha_d)/\tilde{c}}{s\tilde{c}+(G+sC)[1+T^2\tilde{c}(K+sZ)]}. \tag{15}$$

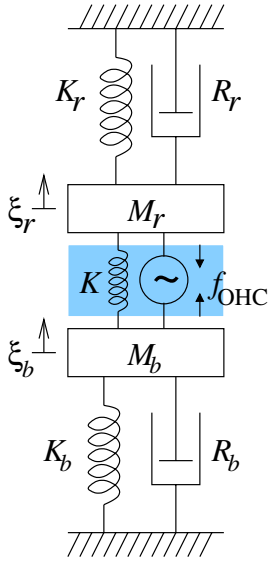

FIG. 4. (Color online) Organ of Corti micro-mechanical model (Lu *et al.*, 2006). The RL system is characterized by parameters $\{K_r, R_r, M_r\}$, the BM system is characterized by parameters $\{K_b, R_b, M_b\}$, and OHC lateral wall (shaded area) is characterized by a contraction force f_{OHC} and a static stiffness K.

The mechanical load impedance Z in Eq. (15) is not defined yet. As illustrated in Fig. 4, let us assume that the OHC contraction force f_{OHC} pulls two systems toward each other: a basilar-membrane (BM) system with an impedance of $Z_b \triangleq s^{-1}K_b + R_b + sM_b$ and a RL system with an impedance of $Z_r \triangleq s^{-1}K_r + R_r + sM_r$ (Lu *et al.*, 2006). Thus, Z can be written as

$$Z = \frac{Z_b Z_r}{Z_b + Z_r}. \tag{16}$$

Equation (16) can be substituted into Eq. (15) to calculate $H_o(s)$. Figures 5(a) and 5(b) show the magnitude and phase response of $H_o(s)$, respectively. The magnitude response of $H_o(j\omega)$ is plotted in logarithmic scale. Below 1 kHz, the magnitude response rolls off at 6 dB/octave due to the RC-filtering of the membrane represented by the term $(G+sC)$ in the denominator of Eq. (15). Between 1 and 4 kHz, the response is relatively flat because the 6 dB/octave roll-off is compensated by a 6 dB/octave gain due to the term $s\alpha_v$ in the numerator of Eq. (15). Between 4 and 16 kHz, the response has two resonance peaks due to the presence of two second-order systems: the RL and the BM. Above 16 kHz, the response rolls off at 12 dB/octave.

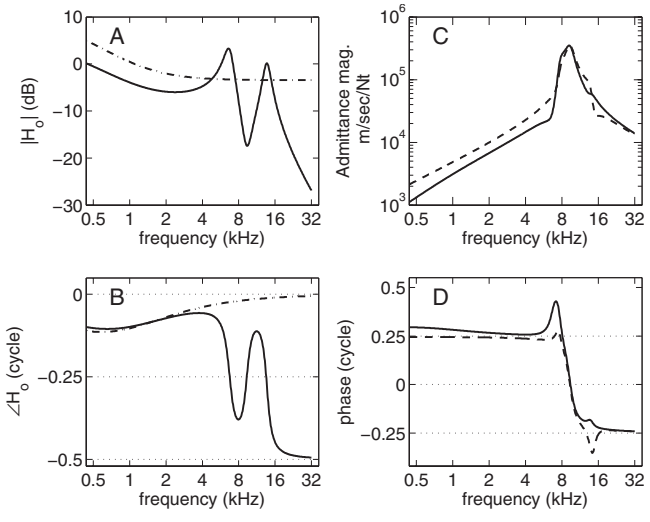

FIG. 5. OHC frequency responses *in situ*. [(A) and (B)] Magnitude and phase of $H_o(s)$. For comparison, dash-dotted curves show results for $Z=0$ (as in an isolated preparation). [(C) and (D)] Magnitude and phase responses, respectively, of velocities $s\xi_r$ (solid) and $s\xi_b$ (dashed) with respect to an externally applied force f_{cp}. Parameters used in this simulation are listed in Table I.

Although the term $s\alpha_v$ compensates for the 6 dB/octave loss of gain due to RC-filtering, there is no guarantee that an OHC gives amplification to cochlear traveling waves. Whether power is dissipated or amplified must be determined by the response of the cochlear partition to a force stimulus. Let us assume that the cochlear partition consisting of the BM system and the RL system is subject to an external force f_{cp}:

$$f_{cp} = Z_b \cdot s\xi_b + Z_r \cdot s\xi_r. \tag{17}$$

Though the preceding equation has two velocity variables $s\xi_b$ and $s\xi_r$, it has only one degree of freedom because the two variables are related in the following manner:

$$s\xi_b = s\xi_r + s\xi_o = [1 + H_o(s)] \cdot s\xi_r. \tag{18}$$

Combining Eqs. (17) and (18), the velocities can be written as a response to the force:

$$s\xi_r = \frac{1}{Z_b(1 + H_o) + Z_r} \cdot f_{cp}, \tag{19}$$

$$s\xi_b = \frac{1 + H_o}{Z_b(1 + H_o) + Z_r} \cdot f_{cp}. \tag{20}$$

The magnitude and phase response of these two velocities with respect to f_{cp} are shown in Figs. 5(c) and 5(d), respectively. The solid curves represent the RL response $s\xi_r/f_{cp}$, and the dashed curves represent the BM response $s\xi_b/f_{cp}$. These responses are referred to as "admittances" because their dimensionality is velocity divided by force. The magnitude responses increase then decrease as a function of frequency, indicating a compliance-dominance at low frequency and a mass-dominance at high frequency. Note that, near 6–8 kHz, the RL admittance phase is more than +0.25 cycle. This corresponds to negative damping, and Sec. IV examines it further.

IV. THE ROLE OF OHCs IN TRAVELING-WAVE AMPLIFICATION

The focus of this section is to calculate the damping coefficient for a one-dimensional, forward-traveling shear wave along the cochlear partition. The traveling of one-dimensional waves can be modeled as propagation in a transmission line, assuming that the canonical variables are pressure difference p across the cochlear partition and volume velocity U along the cochlea (Dallos, 1973, Chap. 4). Fluid

motion inside the organ of Corti, which can be handled by a three-chamber model (Lu *et al.*, 2006), is ignored under the transmission-line assumption.

A. Propagation function $k(s)$ in terms of OHC transfer function $H_o(s)$

At any single location along the cochlea, the damping coefficient $\gamma(s)$ is given as the real part of a propagation function $k(s)$ defined as the following;

$$k = \sqrt{z_{se} y_{sh}} \triangleq \gamma + j\kappa. \tag{21}$$

In the preceding equation, z_{se} and y_{sh} are an acoustic series impedance and an acoustic shunt admittance, respectively. The impedance z_{se} is defined as the pressure gradient $(-\partial_x p)$ divided by U; here, ∂_x denotes partial derivation along the direction of wave propagation. If viscosity of the cochlear fluid can be ignored, z_{se} is given by the following:

$$z_{sc} = s\frac{\rho}{A}, \tag{22}$$

where $\rho = 1.0$ g cm^{-3} is the density of cochlear fluid, and A is the cross-sectional area of the cochlea.

The shunt admittance y_{sh} is defined as the volume-velocity gradient $\partial_x U$ divided by $(-p)$. Let us assume that $\partial_x U$ equals the width W of cochlear partition times the sum of RL and BM velocities; that is,

$$\partial_x U(s) = W \cdot s(\xi_r + \xi_b). \tag{23}$$

For simplicity, also assume that p is a constant radially so that an effective force f_{cp} exerted on an OHC is given by the following;

$$f_{cp} = -p \cdot DW/3, \tag{24}$$

where D is the distance from one OHC to its nearest neighbor in the longitudinal direction, and the factor of 3 is the number of rows of OHCs radially. Combining the two preceding equations, y_{sh} can be written as the following:

$$y_{sh} \triangleq \frac{\partial_x U(s)}{-p(s)} = \frac{DW^2}{3} \cdot \frac{s(\xi_r + \xi_b)}{f_{cp}}. \tag{25}$$

Substituting Eqs. (19) and (20) into Eq. (25), the shunt admittance can be written in terms of the OHC transfer function:

$$y_{sh} = \frac{DW^2}{3} \cdot \frac{2 + H_o(s)}{Z_b(s)[1 + H_o(s)] + Z_r(s)}. \tag{26}$$

Finally, the propagation function $k(s)$ can be calculated by substituting Eqs. (22) and (26) into Eq. (21). The dimensionality of k is cm^{-1}. The real part γ is an attenuation factor, and the imaginary part κ is the wave number. If reverse-traveling waves can be ignored, Neely and Allen (2009) showed that the sign of γ determines whether the forward-traveling waves are attenuated $(\gamma > 0)$ or amplified $(\gamma < 0)$.

Because z_{se} is purely imaginary in Eq. (22), γ in Eq. (21) is negative only if the real part of y_{sh} is negative. Figure 6 shows the real and imaginary parts of y_{sh} and k given by Eqs. (26) and (21), respectively. Figures 6(a) and 6(c) suggest that significant negative damping occurs only when $\alpha_v > 0$. If

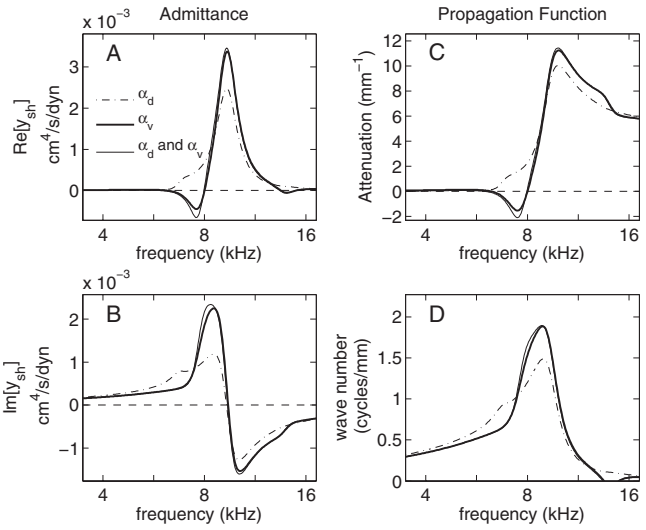

FIG. 6. Acoustic shunt admittance and propagation function as a function of frequency at a single location. [(A) and (B)] Real and imaginary parts of shunt admittance, respectively. [(C) and (D)] Real and imaginary parts of propagation function, respectively. Each panel shows results for three different motion-sensing conditions of the MET: $\alpha_v > 0$, $\alpha_d = 0$ (thick solid curves); $\alpha_v > 0$, $\alpha_d > 0$ (thin solid curves), and $\alpha_v = 0$, $\alpha_d > 0$ (dash-dotted curves).

$\alpha_v > 0$, a nonzero α_d provides a marginal improvement in the depth of negative damping. Also, negative damping occurs within half an octave below the characteristic frequency near 8 kHz, while the wave number κ reaches its maximum at a slightly higher frequency [Fig. 6(d)].

B. Variation in $y_{sh}(s)$ with respect to OHC parameters

The frequency response of shunt admittance $y_{sh}(s)$ is sensitive to OHC parameters. In this section, sensitivities to α_v and $\tilde{c}$ are studied because they represent HB motility and somatic motility, respectively. Figure 7 depicts variation in the real part of $y_{sh}(s)$ with respect to α_v and $\tilde{c}$. For $\tilde{c}$ of 2 pF, negative damping does not occur except for the two highest α_v values. More significant negative damping occurs for $\tilde{c}$ of 5 pF or higher and, as α_v increases, the depth of negative damping first increases (until $\alpha_v/\alpha_{v0} = 4$) and then decreases. For each $\tilde{c}$, the response shifts toward high frequency as α_v increases.

It is of practical interest to quantify the effect of negative damping by measuring its depth and width. The depth of negative damping can be defined as $(-\min \mathrm{Re}[y_{sh}])$, but the width of the negative damping region (NDR) needs to be defined more carefully so it conveys information about the effect size. Figure 8(d) illustrates a reasonable way of defining the width of NDR. The higher boundary of NDR is defined as the highest frequency at which $\mathrm{Re}[y_{sh}] \leq 0$. The lower boundary of NDR is defined via calculation of the slope of $\mathrm{Re}[y_{sh}]$ with respect to $\log f$: the tangential line at the point of maximum negative slope is illustrated by a thin line in Fig. 8(d), and its zero-crossing frequency defines the lower boundary of NDR.

In Figs. 8(a) and 8(b), the width and the depth of NDR are plotted as a function of $\tilde{c}$ for eight discrete values of α_v. For each α_v, negative damping only occurs if $\tilde{c}$ is higher than

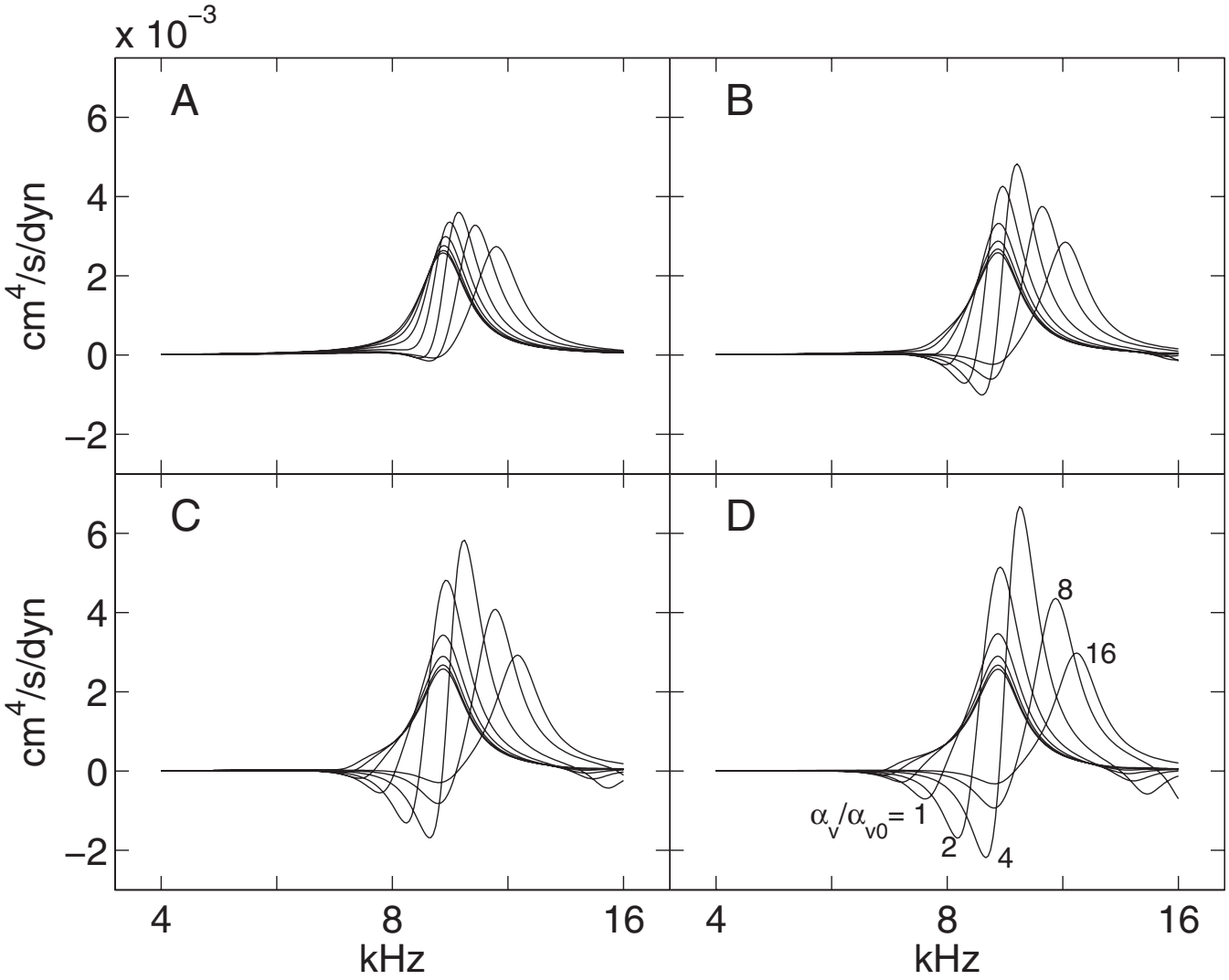

FIG. 7. The real part of shunt admittance y_{sh} as a function of frequency for different combinations of α_v and $\tilde{c}$. Panels (A), (B), (C), and (D) correspond to $\tilde{c}$=2, 5, 10, and 20 pF, respectively. In each panel, eight traces are plotted; from left to right, they correspond to α_v of 0.125, 0.25, 0.5, 1, 2, 4, 8, and 16 times the default $\alpha_{v0}=2.5\times10^{-6}$ C/m. Other parameters are listed in Table I.

a threshold. This threshold ranges from a few picofarads (for the highest α_v) to about 14 pF (for the lowest α_v). Figure 8(c) shows the product of width and depth of NDR. This product can be regarded as a figure of merit to evaluate how much negative damping an OHC provides to the traveling waves. As $\tilde{c}$ increases, the product reaches a plateau, and $\alpha_v=4\alpha_{v0}$ gives the highest plateau value among all choices of α_v.

C. Analytic approximation of shunt admittance $y_{sh}(s)$

Expressions for $y_{sh}(s)$ and $H_o(s)$ derived in Sec. IV A may be simplified to obtain analytic approximations of OHC tuning properties. To do so, note that in Fig. 7, NDR consistently occurs at higher than 6 kHz. At this frequency range, because $\omega \gg G/C$, conductance G can be neglected in Eq. (15). Also, α_d becomes negligible in Eq. (15) if α_v is sufficiently large so that

$$\alpha_v \gg \frac{\alpha_d}{\omega}. \quad \{\text{Assumption\#1}\}$$

Further, because $K_b \gg K_r$, if the frequency range of NDR is sufficiently lower than $\sqrt{K_b/M_b}$, it can be conveniently assumed that

$$|Z_b| \gg |Z_r|, \quad \{\text{Assumption\#2}\}$$

and thus $Z \approx Z_r$ in Eq. (16).

If Assumptions #1 and #2 are both valid, Eq. (15) has the following approximation:

$$H_o(s) \simeq \frac{\alpha_v/TC}{s^2M_r + sR_r + K + K_r + (T^2\tilde{c})^{-1} + (T^2C)^{-1}}. \quad (27)$$

By substituting Eq. (27) into Eq. (26), the following approximation of y_{sh} is obtained;

$$y_{sh}(s) \simeq \frac{DW^2}{3} \cdot \frac{2}{Z_b} \cdot \frac{s^2M_r + sR_r + K_{eq} + \alpha_v/2TC}{s^2M_r + sR_r + K_{eq} + \alpha_v/TC}, \quad (28)$$

where an equivalent stiffness K_{eq} is defined as

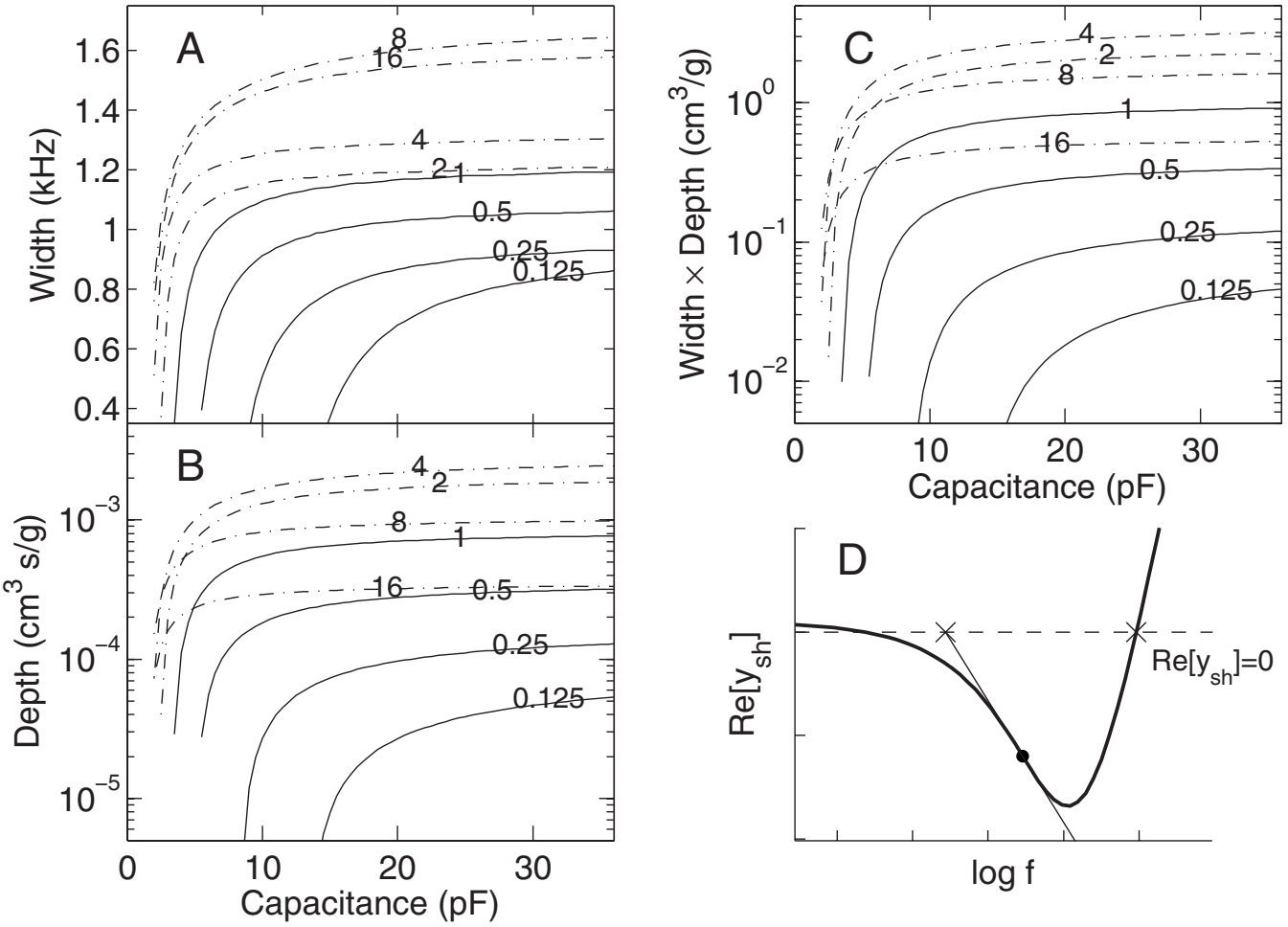

FIG. 8. Quantifying the effect of negative damping. [(A) and (B)] Width and depth, respectively, of NDR as a function of $\tilde{c}$. Each trace is marked by a number indicating the ratio α_v/α_{v0} (0.125, 0.25, etc.). For better viewing, results for $\alpha_v/\alpha_{v0}>1$ are plotted in dashed-dotted lines. Other parameters are listed in Table I. (C) Width times depth of NDR as a function of $\tilde{c}$. (D) Definition of NDR. The dashed line marks zero damping. The crosses mark the boundaries of NDR. The lower boundary is calculated by extending the tangential line from the point of maximum negative slope (marked by a dot).

$$K_{\text{eq}} = K + K_r + (T^2\tilde{c})^{-1} + (T^2 C)^{-1}.$$

In approximation (28), y_{sh} has a resonance frequency $\omega_b = \sqrt{K_b/M_b}$ due to Z_b, a pole frequency $\omega_p = \sqrt{(K_{\text{eq}} + \alpha_v/TC)/M_r}$, and a zero frequency $\omega_z = \sqrt{(K_{\text{eq}} + \alpha_v/2TC)/M_r}$. Note that ω_z is always lower than ω_p. If

$$\frac{K + K_r + 1/T^2\tilde{c} + (1 + T\alpha_v)/T^2 C}{M_r} < \frac{K_b}{M_b},$$

{Assumption#3}

in other words, if ω_p is lower than ω_b, then Z_b is stiffness-dominated at ω_p and y_{sh} has the following approximation:

$$y_{\text{sh}}(j\omega_p) \simeq \frac{DW^2/3}{K_b} \cdot \left(2j\omega_p - \frac{\alpha_v}{TR_r C}\right). \tag{29}$$

Although the approximation in Eq. (29) is rudimentary, it predicts that the real part of y_{sh} is negative at the pole frequency ω_p. This approximation can be refined if ω_p is still lower than but closer to ω_b:

$$y_{\text{sh}}(j\omega_p) \simeq \frac{DW^2/3}{K_b - \omega_p^2 M_b}\left(-\frac{\alpha_v}{TR_r C}(1-\chi) + 2j\omega_p(1+\chi)\right), \tag{30}$$

where

$$\chi = \frac{R_b}{K_b/\omega_p - \omega_p M_b} = \tan\left(\frac{\pi}{2} - \angle Z_b(j\omega_p)\right).$$

The real part of Eq. (30), being negative if $\chi<1$, gives an analytic approximation of the depth of NDR. Figure 9 compares this analytic prediction to numerical calculation of the depth of NDR described in Sec. IV B. The numerical results are obtained with the parameters listed in Table I, except that $\tilde{c}$ is set relatively high at 36 pF to ensure that NDR width reaches the plateau region in Fig. 8(b). Though it is derived under several assumptions, the analytic approximation produces less than 50% of error until α_v exceeds $4\alpha_{v0}$. For $\alpha_v = 8\alpha_{v0}$ and $16\alpha_{v0}$, the approximation fails because Assumptions #2 and #3 are not valid. Particularly, Assumption #3 requires that $\alpha_v < 5.5\alpha_{v0}$ under the present choice of parameter values. As α_v increases beyond, numerical calculation shows that NDR still exists but its depth decreases gradually as a function of α_v.

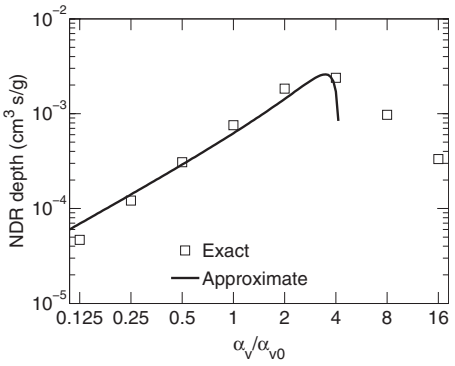

FIG. 9. Analytic approximation of negative damping depth as a function of α_v. The curve shows prediction of the depth given by Eq. (30) if $\tilde{c}$ approaches ∞. The squares show numerical calculation of the depth without simplifying the expression of $H_o(s)$ and $y_{sh}(s)$.

V. DISCUSSION

A. Comparison to other piezoelectric circuit models

Different circuit diagrams to represent OHC piezoelectricity have previously been drawn by Lu *et al.* (2006) and by Allen and Fahey (2006) independently. The model of Lu *et al.* (2006) was linear, and the displacement current i_d was proportional to the time-derivative of OHC external force. Transformers were not explicitly shown in the circuit diagram (Lu *et al.*, 2006, Fig. 18). In Allen and Fahey's (2006) model, it was suggested that nonlinearity be placed in the mechanical compliances so that nonlinear capacitance could be seen as a dual effect via piezoelectricity. In the present model, however, nonlinearity is placed in the capacitance, and nonlinear motility is seen as the dual effect.

The present circuit diagram may look at odds with Allen and Fahey's (2006) suggestion, but the symmetry of Gibbs energy with respect to voltage and force in Eq. (A3) implies that the circuit can be drawn either with a nonlinear compliance or a nonlinear capacitor. By substituting Q in Eq. (2) with Eq. (3), OHC motility ξ_o can be written as

$$\xi_o = \frac{L_{\max}}{1+\exp(f_{\mathrm{OHC}} - V/T - f_0)/f_1}, \tag{31}$$

where $L_{\max}=TQ_{\max}$, and f_0 and f_1 are defined in a similar manner as v_0 and v_1 in Eq. (3). Similar to $\tilde{v}$, a force component can be defined as $\tilde{f}=f_{\mathrm{OHC}}-V/T$. Thus, the circuit in Fig. 1 can be equivalently drawn as Fig. 10, where

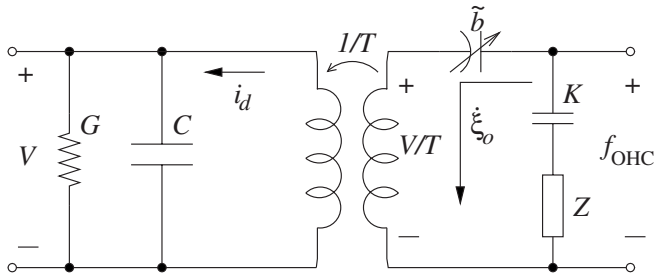

FIG. 10. An equivalent circuit to the proposed model in Fig. 1. The nonlinear component is moved from the electrical to the mechanical domain.

$$\tilde{b} \triangleq \frac{\partial \xi_o}{\partial \tilde{f}} \tag{32}$$

represents a nonlinear compliance. Note that $\tilde{b}$ is equal to $T^2\tilde{c}$ in Eq. (10). Also, when linearized, the circuit diagram in Fig. 10 becomes equivalent to what was presented by Lu *et al.* (2006, Fig. 18).

This circuit is similar to that of Allen and Fahey (2006, Fig. 2) in the sense that the force (or pressure in their case) is loaded with the series connection of a nonlinear compliance and a piezoelectric transformer. However, the model of Allen and Fahey (2006) was more complex because it allowed fluid to flow through the membrane. Such consideration may be important for modeling slower processes.

B. Voltage-dependent cell compliance

The present model cannot explain He and Dallos's (1999) finding of a monotonic decrease in stiffness as a function of membrane potential. Iwasa (2001) suggested that, to explain He and Dallos's (1999) results, the elastic moduli of the membrane motor must differ in its two conformational states. Without this refinement, Iwasa (2001) predicted a maximum axial-compliance increment of 20% as a function of membrane potential, which occurs at the same voltage for peak capacitance. Deo and Grosh (2004) carried out Iwasa's (2001) suggestion by assuming that the membrane motor is stiffer in the extended state than in the compact state and was able to reproduce the results of He and Dallos (1999) in a numerical simulation.

Compared to Iwasa's (2001) prediction, the present model produces similar results for the voltage-dependence of OHC axial-compliance. This is not unexpected because the present model can be derived from a one-dimensional approximation of Eq. (A2) proposed by Iwasa (1993).

Regarding Hallworth's (2007) findings, Dallos (2008) commented that only "healthier" cells demonstrate the voltage-dependent stiffness consistently. One possible explanation is that the membrane potential alters the self-association of motor molecules. A depolarizing (positive) potential works to "cluster" motor molecules and moves the equilibrium in favor of higher oligomeric forms rather than monomers (Rajagopalan *et al.*, 2007). This shift of equilibrium may also give rise to a stiffness decrease when the OHC is depolarized. A recent observation of decoupling between gating charge and motility in a simultaneous measurement (Wang, 2008) may provide more insight on this issue.

Whether or not OHC stiffness is voltage-dependent, cochlear tuning may not be sensitive to it. Note that the value of the axial stiffness K listed in Table I is typical of an OHC from the basal turn of the cochlea (Hallworth, 2007). This K is negligible in Eqs. (15) and (27) at the frequency range of interest (near NDR) because it is much smaller than K_r. Consequently, tuning should not be affected much by the voltage-dependence of OHC stiffness that was observed by He and Dallos (1999).

However, the scenario may be different elsewhere in the cochlea. Empirically, K is inversely proportional to the static length of OHC (Holley and Ashmore, 1988). Therefore, K

can be two to ten times smaller than the present value at more apical locations (He and Dallos, 1999) where OHCs are longer. In contrast, K_b and K_r decrease even more from base to apex by up to 100- to 600-fold near the helicotrema (Naidu and Mountain, 1998; Lu *et al.*, 2006). Because of a higher ratio K/K_r there, K is not negligible in Eq. (15). Consequently, the voltage-dependence of K, or the lack of it, could be an important factor in determining the tuning properties in the apical region of the cochlea.

C. Cochlear amplification: Is receptor current sensitive to RL velocity?

As the present model predicts, negative damping requires that the receptor current be sensitive to RL velocity. Similarly, Lu *et al.* (2009) suggested that a velocity-sensing HB accounts for more cochlear amplification than a displacement-sensing HB.

Experiments have shown that the receptor current has a fast adaptation to a step deflection in the HB (Fettiplace *et al.*, 2006). In other words, the current has a low-pass filtered response to a velocity impulse. By inspection, the velocity-sensing gain measured in the experiments was about 0.25 pA/μm s [Fettiplace *et al.*, 2006, Fig. 2(B)]. This estimate is conservative because the time-constant of adaptation was too short to be measured by the devices. Fettiplace *et al.* (2006) also suggested that the receptor current *in vivo* should be about four fold larger than measured in isolated OHC because of a higher endolymphatic potential and potassium as the major cation. This would partially eliminate the order-of-magnitude difference between their data and the default α_{v0} value listed in Table I. Nevertheless, one should remain cautious that the value of α_{v0} used in the present study may be unrealistically high.

In Eq. (14), a heuristic relation between the receptor current and the RL motion is described. A reasonable interpretation of the equation is that the TM is radially rigid, and HB deflection is directly proportional to RL displacement. Under this interpretation, Eq. (14) states that the receptor current is the sum of a response to HB deflection plus a fast adaptive component.

An alternative interpretation is that the receptor current responds to the angle of HB deflection only, but the current is effectively sensitive to RL velocity via the interaction between the HB and a non-rigid TM. Let ξ_t denote the displacement of TM and ζ denote the deflection angle of HB, which is proportional to $\xi_r - \xi_t$ (ξ_r being RL displacement). At high frequency when the mass of TM dominates, ξ_t is approximately zero and ζ is proportional to ξ_r. At a lower frequency, it is conceivable that the phase of ξ_t may lag behind that of ξ_r, giving rise to a phase lead of ζ relative to ξ_r. If this happens, there would be a component of HB deflection that is in-phase with RL velocity. Thus, cochlear amplification would not require fast adaptation of MET. However, details of TM mechanics are beyond the scope of the present study.

Evidence of cochlear traveling-wave amplification has been presented via solution of an inverse-scattering problem (Shera, 2007). The propagation function k was estimated from auditory-nerve recording data (e.g., Temchin *et al.*, 2005; van der Heijden and Joris, 2006), and results indicate that negative damping must have occurred at basal, middle, as well as apical locations in the cochlea (Shera, 2007, Fig. 8). The present prediction of k as a function of frequency [Figs. 6(c) and 6(d)] is similar to Shera's (2007) estimation inasmuch as, first, that negative damping occurs below the best frequency; second, the peak of $\kappa(\omega)$ occurs near the zero-crossing frequency of $\gamma(\omega)$; finally, the width of NDR is less than half of an octave [Fig. 8(b)]. These similarities suggest that the present OHC model may be useful for describing active wave propagation in the cochlea. Also, analyses described in Sec. IV predict the sensitivity of the width and depth of NDR to OHC parameters in specific ways. These predictions can thus be verified or refuted via experimental means.

ACKNOWLEDGMENTS

This study was supported by a grant from NIH-NIDCD (Contract No. R01-DC8318).

APPENDIX: FOUNDATION IN STATISTICAL MECHANICS

Piezoelectric models of the OHC (e.g., Mountain and Hubbard, 1994; Tolomeo and Steele, 1995) can be derived from thermodynamic principles if Gibbs free energy is known. The simplest form of Gibbs free energy was proposed by Iwasa (1993) under the following assumptions: (a) the membrane is embedded with motors that have one contracted state and one extended state that differ in area by $\Delta a < 0$ and (b) the change in area is coupled by a charge transfer $\Delta q > 0$. Thus, the probability P_s of any motor unit being in the contracted state is given by the Maxwell–Boltzmann distribution,

$$P_s = \frac{1}{1 + \exp\left[\dfrac{\Delta G}{k_B T_0}\right]}, \tag{A1}$$

where $k_B = 1.38 \times 10^{-23}$ J/deg is the Boltzmann constant, T_0 is the absolute temperature, and ΔG is the difference of Gibbs free energy between the two states. Iwasa (1993) showed that, if the surface tension on the membrane is isotropic, ΔG is given by the following equation:

$$\Delta G = \Delta G_0 - \Delta q \cdot V - \Delta a \cdot \tau, \tag{A2}$$

where ΔG_0 is a constant, V is the membrane potential, and τ denotes the surface tension on the membrane. Note that, in Eq. (A2), the term $(-\Delta a) \cdot \tau$ is the required mechanical energy for a motor to make a transition from the extended state to the contracted state.

In this study, the nonlinearity in the piezoelectric membrane is described by Eq. (3). The equation can be derived by considering a one-dimensional approximation of Eq. (A2). Imagine that all the motors are identical and aligned in the axial direction and can contract or stretch, as shown in Fig. 11. Assume that the contracted state and the extended state differ by $\Delta l < 0$ in length. Thus, the required mechanical energy to make a transition from the extended state to the contracted state can be written as $(-\Delta l) \cdot f_{\mathrm{OHC}}$, where f_{OHC}

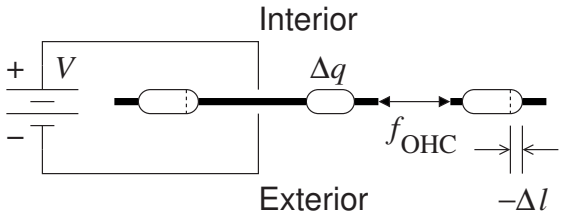

FIG. 11. Illustration of a one-dimensional model of piezoelectric motors embedded in the OHC lateral membrane. Of the three motors shown, two are in the extended state and the middle one is in the contracted state.

denotes the tensile force on the membrane. Hence, the difference in Gibbs energy between the two states is written as the following:

$$\Delta G = \Delta G_0 - \Delta q \cdot V - \Delta l \cdot f_{\mathrm{OHC}}. \tag{A3}$$

The total gating charge Q of an OHC that has N motor units on its lateral membrane is written as

$$Q = N\Delta q \cdot P_s. \tag{A4}$$

Combining Eqs. (A1), (A3), and (A4), Q can be written as a function of V and f_{OHC} in Eq. (3). The macroscopic parameters in Eq. (3) are related to the microscopic parameters in the following ways: $Q_{\max}=N\Delta q$, $T=-\Delta l/\Delta q$, $v_0=\Delta G_0/\Delta q$, and $v_1=k_{\mathrm{B}}T_0/\Delta q$.

[1]For simplicity, DC components such as the resting potential and the turgor pressure are not shown.

Adachi, M., and Iwasa, K. H. (**1999**). "Electrically driven motor in the outer hair cell: Effect of a mechanical constraint," Biophys. J. **96**, 7244–7249.

Allen, J. B., and Fahey, P. F. (**2006**). "Outer hair cell mechanics reformulated with acoustic variables," *Auditory Mechanisms: Processes and Models* (World Scientific, Singapore), pp. 194–201.

Ashmore, J. F. (**1987**). "A fast motile response in guinea-pig outer hair cells: The cellular basis of the cochlear amplifier," J. Physiol. (London) **388**, 323–347.

Brownell, W. E., Bader, C. R., Bertrand, D., and de Ribaupierre, Y. (**1985**). "Evoked mechanical responses of isolated cochlear hair cells," Science **227**, 194–196.

Cooper, N. P. (**1998**). "Harmonic distortion on the basilar membrane in the basal turn of the guinea-pig cochlea," J. Physiol. (London) **509**, 277–288.

Dallos, P. (**1973**). *The Auditory Periphery: Biophysics and Physiology* (Academic, New York).

Dallos, P. (**2008**). "Cochlear amplification, outer hair cells and prestin," Curr. Opin. Neurobiol. **18**, 370–376.

de Boer, E., and Nuttall, A. L. (**2000**). "The mechanical waveform of the basilar membrane. III. Intensity effects," J. Acoust. Soc. Am. **107**, 1497–1507.

Deo, N., and Grosh, K. (**2004**). "Two-state model for outer hair cell stiffness and motility," Biophys. J. **86**, 3519–3528.

Fettiplace, R., Crawford, A. C., and Kennedy, H. J. (**2006**). "Signal transformation by mechanotransducer channels of mammalian outer hair cells," *Auditory Mechanisms: Processes and Models* (World Scientific, Singapore), pp. 245–253.

Hallworth, R. (**2007**). "Absence of voltage-dependent compliance in high-frequency cochlear outer hair cells," J. Assoc. Res. Otolaryngol. **8**, 464–473.

He, D. Z. Z., and Dallos, P. (**1999**). "Somatic stiffness of cochlear outer hair cells is voltage-dependent," Proc. Natl. Acad. Sci. U.S.A. **96**, 8223–8228.

Holley, M. C., and Ashmore, J. F. (**1988**). "A cytoskeletal spring in cochlear outer hair cells," Nature (London) **335**, 635–637.

How, J., Elliott, S. J., and Lineton, B. (**2009**). "The influence on predicted harmonic generation of the position of the nonlinearity within micromechanical models," in *Concepts and Challenges in the Biophysics of Hearing*, edited by N. P. Cooper and D. T. Kemp (World Scientific, Singapore), pp. 350–351.

Hudspeth, A. J. (**1997**). "Mechanical amplification of stimuli by hair cells," Curr. Opin. Neurobiol. **7**, 480–486.

Iwasa, K. H. (**1993**). "Effect of stress on the membrane capacitance of the auditory outer hair cell," Biophys. J. **65**, 492–498.

Iwasa, K. H. (**2001**). "A two-state piezoelectric model for outer hair cell motility," Biophys. J. **81**, 2495–2506.

Iwasa, K. H., and Adachi, M. (**1997**). "Force generation in the outer hair cell of the cochlea," Biophys. J. **73**, 546–555.

Lu, S., Mountain, D., and Hubbard, A. (**2009**). "Is stereocilia velocity or displacement feedback used in the cochlear amplifier?," in *Concepts and Challenges in the Biophysics of Hearing*, edited by N. P. Cooper and D. T. Kemp (World Scientific, Singapore).

Lu, T. K., Zhak, S., Dallos, P., and Sarpeshkar, R. (**2006**). "Fast cochlear amplification with slow outer hair cells," Hear. Res. **214**, 45–67.

Mountain, D. C., and Hubbard, A. E. (**1994**). "A piezoelectric model of outer hair cell function," J. Acoust. Soc. Am. **95**, 350–354.

Naidu, R. C., and Mountain, D. C. (**1998**). "Measurements of the stiffness map challenge a basic tenet of cochlear theories," Hear. Res. **124**, 124–131.

Neely, S. T. (**1985**). "Mathematical modeling of cochlear mechanics," J. Acoust. Soc. Am. **78**, 345–352.

Neely, S. T., and Allen, J. B. (**2009**). "Retrograde waves in the cochlea," in *Concepts and Challenges in the Biophysics of Hearing*, edited by N. P. Cooper and D. T. Kemp (World Scientific, Singapore).

Patuzzi, R. (**1996**). "Cochlear micromechanics and macromechanics," in *The Cochlea*, edited by P. Dallos, A. N. Popper, and R. R. Fay (Springer, New York), pp. 186–257.

Rajagopalan, L., Greeson, J. N., Xia, A., Liu, H., Sturm, A., Raphael, R. M., Davidson, A. L., Oghalai, J. S., Pereira, F. A., and Brownell, W. E. (**2007**). "Tuning of the outer hair cell motor by membrane cholesterol," J. Biol. Chem. **282**, 36659–36668.

Ramamoorthy, S., Deo, N. V., and Grosh, K. (**2007**). "A mechano-electro-acoustical model for the cochlea: Response to acoustic stimuli," J. Acoust. Soc. Am. **121**, 2758–2773.

Ren, T., and Nuttall, A. L. (**2001**). "Basilar membrane vibration in the basal turn of the sensitive gerbil cochlea," Hear. Res. **151**, 48–60.

Robles, L., and Ruggero, M. A. (**2001**). "Mechanics of the mammalian cochlea," Physiol. Rev. **81**, 1305–1352.

Ruggero, M. A., Rich, N. C., Robles, L., and Shivapuja, B. G. (**1990**). "Middle-ear response in the chinchilla and its relationship to mechanics at the base of the cochlea," J. Acoust. Soc. Am. **87**, 1612–1629.

Santos-Sacchi, J. (**1991**). "Reversible inhibition of voltage-dependent outer hair cell motility and capacitance," J. Neurosci. **11**, 3096–3110.

Shera, C. A. (**2007**). "Laser amplification with a twist: Traveling-wave propagation and gain functions from throughout the cochlea," J. Acoust. Soc. Am. **122**, 2738–2758.

Spector, A. A., Brownell, W. E., and Popel, A. S. (**1999**). "Nonlinear active force generation by cochlear outer hair cell," J. Acoust. Soc. Am. **105**, 2414–2420.

Spector, A. A., Deo, N., Grosh, K., Ratnanather, J. T., and Raphael, R. M. (**2006**). "Electromechanical models of the outer hair cell composite membrane," J. Membr. Biol. **209**, 135–152.

Temchin, A. N., Recio-Spinoso, A., van Dijk, P., and Ruggero, M. A. (**2005**). "Wiener kernels of chinchilla auditory-nerve fibers: Verification using responses to tones, clicks, and noise and comparison with basilar-membrane vibrations," J. Neurophysiol. **93**, 3635–3648.

Tinevez, J.-Y., Jülicher, F., and Martin, P. (**2006**). "Unifying the various incarnations of active hair-bundle motility by the vertebrate hair cell," Biophys. J. **93**, 4053–4067.

Tolomeo, J. A., and Steele, C. R. (**1995**). "Orthotropic piezoelectric properties of the cochlear outer hair cell wall," J. Acoust. Soc. Am. **97**, 3006–3011.

van der Heijden, M., and Joris, P. X. (**2006**). "Panoramic measurements of the apex of the cochlea," J. Neurosci. **26**, 11462–11473.

Wang, X. (**2008**). "Outer hair cell electromotility and cochlear amplifier," Ph.D. thesis, Creighton University, Omaha, NE.

Weitzel, E. K., Tasker, R., and Brownell, W. E. (**2003**). "Outer hair cell piezoelectricity: Frequency response enhancement and resonance behavior," J. Acoust. Soc. Am. **114**, 1462–1466.